ELSEVIER

Journal of Nuclear Materials 313–316 (2003) 804–812

journal of nuclear materials

www.elsevier.com/locate/jnucmat

A review of plasma boundary phenomena in the mega ampere spherical tokamak

G.F. Counsell [a,*], J.-W. Ahn [a], R. Akers [a], E. Arends [b], S.J. Fielding [a], P. Helander [a], A. Kirk [a], H. Meyer [a], A. Tabasso [a], H. Wilson [a], Y. Yang [c]

[a] *Euratom/UKAEA Fusion Association, Culham Science Centre, D3/022 Abingdon, Oxon OX14 3DB, UK*
[b] *FOM Institute for plasma physics 'Rijnhuizen', P.O. Box 1207, 3430 B Nieuwegein, The Netherlands*
[c] *Institute of Plasma physics, Hefei 230031, PR China*

Abstract

Enhanced diagnostics and an expanded operational space in Mega Ampère Spherical Tokamak (MAST) has lead to a wealth of data on the plasma boundary becoming available over the last year of operations and has significantly advanced the understanding of this region in the spherical tokamak and, more generally, is contributing to an improved understanding of the underlying plasma phenomena for this important region of the tokamak. Amongst the observations reported in this paper are that MAST is able to achieve simultaneous high confinement and high density with Type III ELMs for connected double-null discharges in which most (>93%) of the power efflux from the core observed at the targets (including during ELMs) arrives at the large wetted area outboard targets and is evenly distributed between the upper and lower divertor regions. Significant particle fluxes are reported well beyond the outboard separatrix during ELMs (up to 20 cm distant from the plasma) and appear to be associated with the radial expansion of a localised structure at around 1 km s^{-1}. The result of preliminary experiments to broaden the SOL by asymmetric divertor biasing are also presented which show an encouraging, qualitative agreement with theory and demonstrate clear evidence for both SOL broadening and target power reduction.

Keywords: Spherical tokamak; Scrape-off layer; ELM; Divertor biasing; Power balance

1. Introduction

The study of plasma edge phenomena in the spherical tokamak (ST), and their relation to those observed in conventional devices, has been a key research topic for the Mega Ampère Spherical Tokamak, MAST, since the start of operations in 2000. Recent improvements to the auxiliary heating and gas fuelling systems have broadened the operational space of MAST and, together with a range of new and enhanced diagnostics, has led to a wealth of data on the plasma boundary becoming available. Analysis of these data are contributing not only to better characterisation of the ST plasma edge and exhaust but also to improved understanding of the physics underlying this region in general. This paper presents a review of observations and modelling of the plasma boundary, divertor and plasma-surface interaction region in MAST.

2. Background

MAST has a major radius, $R \sim 0.85$ m, and a minor radius, $a \sim 0.65$ m. It has operated with plasma current up to $I_p \sim 1.2$ MA and is equipped with two neutral beam lines, which have so far provided hydrogen and deuterium injection into plasma with powers in excess of $P_{NBI} \sim 2.5$ MW (although they will eventually be

* Corresponding author. Tel.: +44-1 235 466602; fax: +44-1 235 466511.
E-mail address: glenn.counsell@ukaea.org.uk (G.F. Counsell).

0022-3115/03/$ - see front matter
PII: S0022-3115(02)01439-3

capable of up to 5 MW). The toroidal field varies between around 2 T at the inboard mid-plane to 0.25 T at the outboard, with the toroidal field on axis, B_ϕ usually in the range 0.35–0.55 T. MAST typically has an asymmetric double-null divertor configuration in which the outer strike-points (both upper and lower) fall onto two sets of 12, toroidally discrete, radial graphite ribs mounted horizontally at the top and bottom of the vessel. The inner strike-points fall onto toroidally continuous graphite armour protecting the vessel centre column. A separatrix is associated with each magnetic null and the degree of magnetic asymmetry is characterised by the separation, $\delta r_{\rm sep}$, of the inner and outer separatrices at the mid-plane. Discharges in which the outboard $\delta r_{\rm sep}$ is very much less than the heat flux width in the scrape-off layer (SOL) are referred to as connected double-null, CDN (typically $\delta r_{\rm sep} < 3$ mm in CDN). $\delta r_{\rm sep}$ can be varied from around −15 mm (for which little energy or particle flux reaches the upper divertor and thus resemble lower single-null divertor, LSND, operation) to +15 mm (resembling upper single-null divertor, USND, operation).

All four targets are equipped with arrays of flush mounted Langmuir probes (over 400 in all) giving a spatial resolution, flux-mapped to the mid-plane, of around 2–3 mm for both the inboard and outboard SOL. D_α light from each target is collected by a filtered photomultiplier and a spectrometer is used to simultaneously resolve D_α and D_γ emission at any one target. D_α emission from the plasma edge at the mid-plane is collected with a filtered linear camera, giving a spatial resolution of better than 2 mm. The outboard mid-plane SOL is accessed by a fast reciprocating probe system equipped with a radial array of triple probes and a Mach probe. A 300-point, single pulse Thomson scattering system provides a spatial resolution across the boundary plasma region of around 3 mm.

3. Power balance and accounting

The difference between the wetted area of the inboard and outboard targets in an ST is far more significant than in conventional devices. In MAST, the outboard strike-point region typically has an area 40 times that of the inboard and is two orders of magnitude larger in some designs for future, power plant STs. As a result, considerable attention has been paid to understanding the distribution of power between the four targets in MAST [1,2].

The power arriving at each of the target probes, $P^{\rm t}$, is evaluated from the saturation current, $j_{\rm s}$, and electron temperature, $T_{\rm e}$, using $P^{\rm t} = \gamma k T_{\rm e} j_{\rm s}/e$, taking the sheath transmission coefficient $\gamma = 7$ (sum of the electron and ion sheath transmission coefficients estimated for deuterium ions and a graphite target, assuming $T_{\rm i} \sim T_{\rm e} \sim 20$ eV and accounting for secondary electron emission, electron–ion recombination, ion particle and energy reflection coefficients but ignoring molecular recombination, from [3]). The total power flowing to each target, $P_{\rm tot}$, is obtained both by summing over all probes in the strike-point region and by fitting the SOL and private flux regions on either side of the strike-point with exponentials (and integrating), the two methods typically agreeing to within 10%. For L-mode and ELMy H-mode regimes, the sum of $P_{\rm tot}$ over all four targets typically represents more than 80% of the power estimated to be flowing from the core, allowing for radiation and changes in stored energy. This fraction does appear to fall during long inter-ELM periods, possibly as the result of an increase in SOL ion temperature and a corresponding rise in power flowing in the ion channel, to which the target probes are insensitive.

$P_{\rm tot}$ was calculated at each target for a series of 600 kA Ohmic plasmas, whilst $\delta r_{\rm sep}$ in the 'flat-top' phase was varied on a shot by shot basis from around −15 to 15 mm (LSND to USND) [2]. In the single-null divertor, SND, configurations the bulk of power and particles flowed to the corresponding targets (lower or upper) as expected. The ratio of power to the lower targets compared to the upper, $R_{\rm lu}$, was typically 20:1 in LSND and 1:6 in USND, the asymmetry probably arising from the influence on the ion $\nabla B/B$ drift (towards the lower X-point). In these Ohmic SND plasmas, the ratio of power to the outboard targets compared to the inboard, $R_{\rm oi}$, was ∼4:1 (Fig. 1), that is around 80% of power observed at the targets arriving to the outboard. Only L-mode regimes were encountered for large values of $|\delta r_{\rm sep}|$ (SND plasmas) but H-mode access was achieved for CDN configurations, with $|\delta r_{\rm sep}| <\sim 3$ mm. Similar behaviour was observed for auxiliary heated plasmas, even up to the maximum $P_{\rm NBI}$ available.

For CDN plasmas, $R_{\rm lu}$ was reduced to less than 1.5:1 and reached unity (i.e. balanced power between the upper and lower targets) for $\delta r_{\rm sep} \sim 2$ mm (rather than $\delta r_{\rm sep} = 0$, again probably due to the ion $\nabla B/B$ drift). $R_{\rm oi}$ exceeded 25:1 for Ohmic L-mode plasmas and at ELM peaks in Ohmic H-mode plasmas but fell to around 10:1 during inter-ELM periods. For auxiliary heated plasmas, which exhibit lower ELM frequency (see Section 4.1) and longer inter-ELM periods, $R_{\rm oi}$ falls even further, to around 4:1, comparable with the ratio of surface areas for the outboard and inboard separatrices. The data is consistent with losses from the core being driven by poloidally symmetric processes during inter-ELM periods, and thus distributed according to the area ratio. During L-mode periods and at ELM peaks, the transport is presumably enhanced by poloidally asymmetric processes more prominent in the low field, bad curvature outboard side.

The target power balance observed in MAST is potentially rather favourable for the ST since H-mode

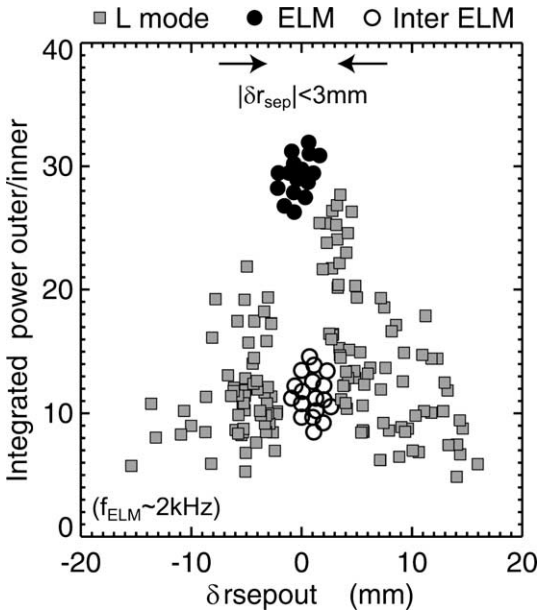

Fig. 1. Ratio of total power arriving at the outboard targets compared to the inboard as a function of magnetic asymmetry in L-mode and ELMy H-mode regimes for a series of 600 kA, Ohmic plasmas. $|\delta\text{rsepout}| \sim 15$ mm represents quasi-SND (upper and lower) operation and $|\delta\text{rsepout}| <\sim 3$ mm represents CDN operation.

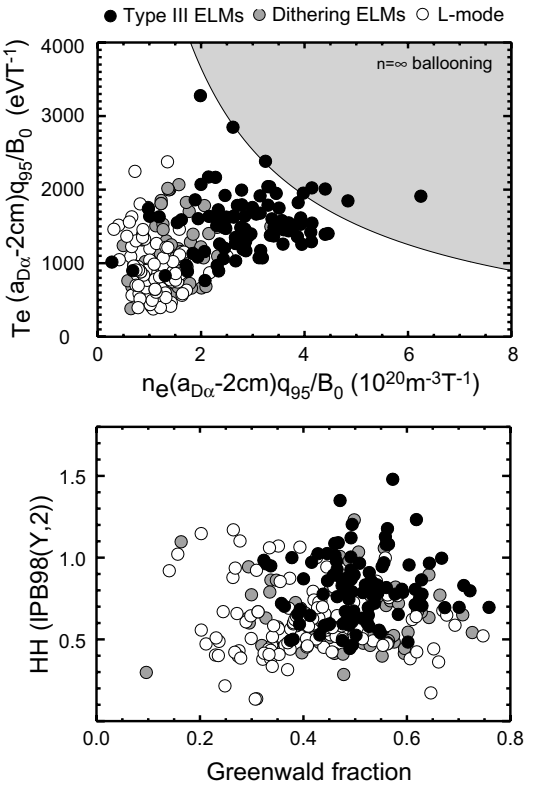

Fig. 2. (a) Edge T–n space (normalised to B_0/q_{95}) and (b) core τ_E–n space (normalised to IPB(y,2) scaling and the Greenwald density, respectively) showing the existence of L-modes and ELMy H-modes from analysis of over 2500 shots. The region of instability to $n = \infty$ ideal ballooning is shaded in (a). The edge T and n were derived from the outboard Thomson scattering profile at 2 cm inboard of the peak in edge D_α emission – found empirically on MAST to provide a robust estimate of the pedestal radius in H-mode discharges.

access is facilitated in a region where ELM losses flow mostly to the large wetted area, outboard targets and, in addition, the target heat loads are reduced by an even distribution of power between the upper and lower targets.

4. Edge localised modes

4.1. ELM characterisation

For fixed power flow across the separatrices, P_{SOL} the ELM frequency, f_{ELM} so far observed in MAST falls with increasing core line averaged density, $\bar{n}_e$. For fixed $\bar{n}_e$, f_{ELM} falls with increasing P_{SOL} [2], a characteristic feature of Type III ELMs in conventional tokamaks. In order to further characterise these ELMs, the edge electron temperature, T_p was plotted against edge density, n_p (indicative of temperature and density gradients in the edge) for a range of discharges featuring L-mode regimes, 'dithering' ELMs and clearly defined ELMs (Fig. 2(a)). T_p and n_p were evaluated from the high resolution Thomson scattering data at a location 2 cm inboard of the radius of peak D_α emission from the outboard mid-plane, r_{D_α} determined using Abel inversion of data from the mid-plane linear D_α camera. The radius r_{D_α}-2 cm is found empirically to provide a robust estimate for the location of the pedestal in MAST H-mode regimes, determined using a modified hyperbolic tangent fit to the Thomson scattering data in the pedestal region.

Data for L-mode regimes are restricted to a region of T_p–n_p space with $n_p <\sim 1.5 \times 10^{19}$ m^{-3} and $T_p <\sim 180$ eV. Despite the ease of access to L-modes with densities close to the Greenwald density, n_G (see later), no L-modes were recorded in this sample of over 2500 discharges with n_p greater than about 1.7×10^{19} m^{-3}, a result of very shallow density gradients at the edge in high density L-mode MAST discharges. Data for ELMy phases of H-mode regimes form a continuum from the L-mode data to higher n_p (up to 5.5×10^{19} m^{-3}) but are similarly restricted in T_p, with no discharges recorded with T_p above 200 eV. Both the ELMy H-mode and L-mode data may also be bounded above a line representing constant $T_p/n_p \sim 3 \times 10^{18}$ eV m^3, possibly indicating that operation with low temperature and high

density is precluded by radiative instabilities for the range of T_p and n_p explored. MHD stability calculations indicate that the ELMy H-mode data is just reaching a boundary associated with the high n ideal ballooning mode limit, at which one would expect to see signs of Type I ELM behaviour. Thus, although the bulk of ELMy H-modes in MAST exhibit ELMs with a Type III character, it is possible that Type I ELMs may exist for discharges at the highest β_N ($\equiv \beta/(I_p/aB)$, where B is the magnetic field at the geometric axis). This will be explored further in the future.

The normalised confinement time H_H ($\equiv \tau_E/\tau_E^{IPB(y,2)}$, where τ_E is the confinement time and $\tau_E^{IPB(y,2)}$ is the estimated confinement time from the IPB(y,2) scaling [4]) has been plotted against the Greenwald fraction, $G = \bar{n}_e/n_G$ (Fig. 2(b)) for the same shots and at the same times as the data presented in Fig. 2(a). ELMy H-modes are readily accessible with both high confinement, $H_H \sim 1$ and high density, $G \sim 0.65$. These discharges have $f_{ELM} <\sim 100$ Hz (an inverse relationship between H_H and f_{ELM} has been previously reported [5]) but the ELMs are still relatively benign, with ELM energy losses representing only 2–3% of stored energy and giving rise to peak target powers of less than 5 MW m^{-2} (a detailed discussion of ELM energy losses in MAST can be found in [2]).

MAST is able to access ELMy regimes with high confinement relative to international scalings, densities at a significant fraction of the Greenwald limit and with 'small' ELMs (releasing less than 2.5% of the stored energy) up to the maximum P_{NBI} so far explored.

4.2. Impact of ELMs on the pedestal profile

The impact of ELMs on the temperature and density profiles in the pedestal region has been evaluated using the single pulse, high resolution Thomson scattering system in a controlled set of 'identical' H-mode discharges with $I_p \sim 650$ kA, $P_{NBI} \sim 0.8$ MW and $f_{ELM} \sim 400$ Hz. Random delays between the ELM times and the Thomson scattering time in each discharge were used to construct the evolution of the pedestal profiles with a coarse time resolution. Due to the long inter-ELM period (2.5 ms, compared to the ELM duration of ~300 μs) and the need to select ELMs from a very narrow range of core plasma parameters, only three shots were suitable for this analysis, with Thomson scattering times at 1580 ms after (≡770 μs before) (shot 5752), 5 μs before (shot 5756) and 340 μs after (shot 5757) the peak target D_α emission. The temperature and density profiles, overlayed with modified hyperbolic tangent fits, are shown in Fig. 3 together with target D_α emission from a representative ELM indicating the relative times at which the profiles were obtained.

At t_{ELM} −770 μs the core density profile is very flat with a steep edge density gradient and a pedestal density

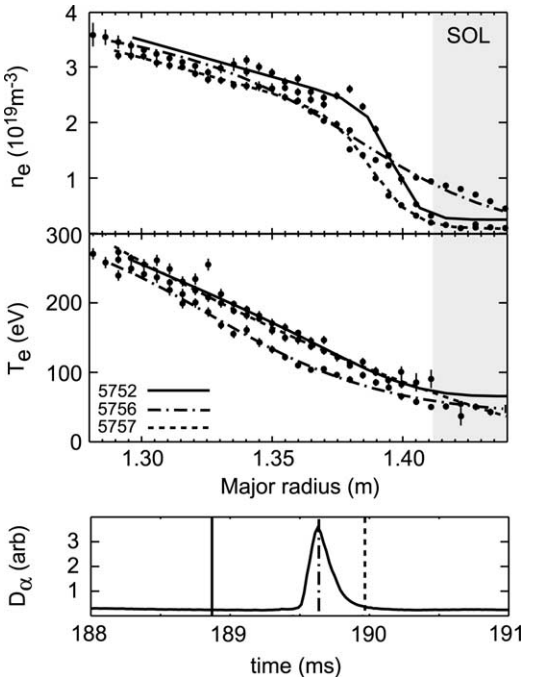

Fig. 3. Thomson scattering profiles of the outboard edge density and temperature for three 'idential' 650 kA, H-mode discharges, with 0.8 MW of neutral beam heating, at three times with respect to a similar ELM in each discharge (divertor D_α emission, lower trace); −770 μs, −5 μs and +340 μs.

of $n_{ped} \sim 2.2 \times 10^{19}$ m^{-3}. In contrast the core temperature profile is rather peaked with a flat edge gradient and little discernible temperature pedestal (the temperature at the radius of the density pedestal, r_{ped} being $T_{ped} \sim 120$ eV). At t_{ELM} −5 μs, during the rapid rise in target D_α emission, the edge density gradient collapses to L-mode levels with no discernible pedestal. The density falls by around 40% at r_{ped} but rises at the inter-ELM separatrix radius, r_{sep} by a factor 5 (to around 1×10^{19} m^{-3}) and a broad tail forms, extending at least 5 cm beyond r_{sep}. The temperature profile remains flat in this phase of the ELM but is reduced by around 20 eV across the pedestal region. By t_{ELM} +340 μs, the foot of the tail in target D_α emission, the temperature profile has completely recovered to inter-ELM values, a steep density gradient has begun to re-form and the outboard tail in the density profile has vanished but n_{ped} is still lower than the inter-ELM value by 15–20%.

The data is consistent with ELM losses in MAST being driven predominantly by convective transport, as might be expected in any case from the lack of a clear temperature pedestal. As a result of the flat core density profile and steep edge density gradient, ELM energy losses, ΔW_{ELM} are strongly correlated to the pedestal density (Fig. 4). However, no correlation is observed

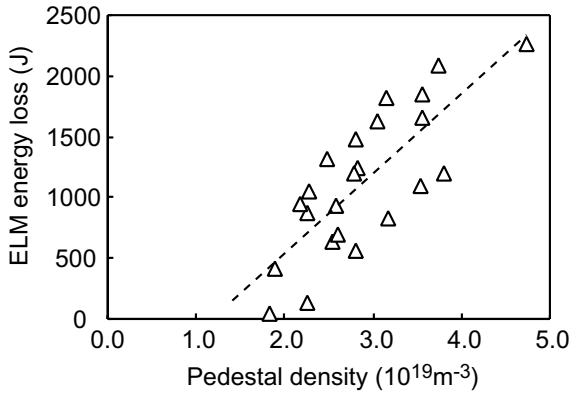

Fig. 4. Energy loss from the core plasma during ELM events, (derived from EFIT) as a function of the pedestal density.

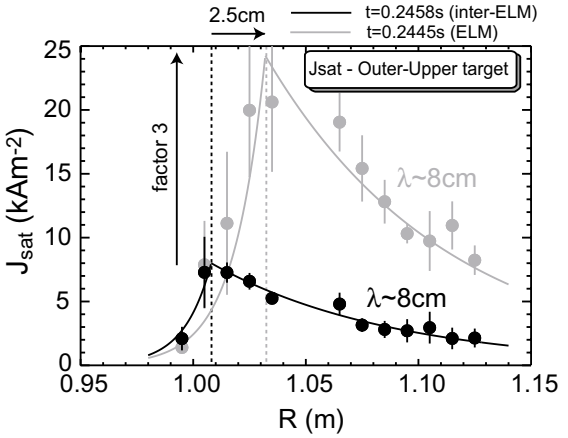

Fig. 5. Profiles of ion saturation current, j_{sat} from the upper, outboard target at two times, just before an ELM and at the peak of the ELM. At the ELM, the peak j_{sat} rises by a factor 3 and shifts 2.5 cm out but the width is un-affected.

between ΔW_{ELM} as a fraction of the pedestal energy, ΔW_{ped} and pedestal collisionality, as reported for a range of conventional tokamaks [6]. Due to the low T_{ped} and high n_{ped} encountered so far in MAST ELMy H-modes with up to $P_{NBI} \sim 2$ MW, pedestal collisionalities are high, between $1 < v^*_{ped} < 3$ and $\Delta W_{ELM}/\Delta W_{ped}$ varies from 1% to 16%. The lack of correlation with v^*_{ped} may be a result of the convective nature of the ELMs observed on MAST and the absence of a significant temperature pedestal in the H-mode regimes so far explored. This indicates that additional parameters may be required to provide a robust extrapolation to ELM energy losses on ITER.

4.3. Characteristics of ELMs at the target

As mentioned in Section 3, the bulk of energy released during ELMs arrives to the outboard targets in CDN (the only divertor geometry for which H-modes have been observed so far). Even for H-modes with high P_{NBI} and low f_{ELM}, where the outer to inner power ratio, R_{oi} falls to around ~14:1, more than 93% of ELM energy observed at the targets is to the outboard side. The outboard strike-points shift radially outward (at both the upper and lower targets) during these low frequency ELMs, by up to around 3 cm or 30–40% of the target heat flux width (Fig. 5). The movement occurs rapidly, within the first 50–100 μs or so at the beginning of the ELM. There is, however, no significant broadening of the target SOL width during the ELM.

Strike-point movement during ELMs could be a significant challenge if observed in ITER, where the targets are near vertical. A radial shift of several centimetres would result in a vertical shift of many 10's of centimetres, potentially moving the strike-points onto plasma-facing components un-able to withstand ELM heat fluxes.

4.4. Observations of ELMs in the outboard mid-plane SOL

Observations of significant power and particle efluxes well beyond the outboard separatrix during ELMs in MAST have been reported elsewhere [1], but have now been characterised in greater detail [7]. Strong interactions are regularly observed with the outboard mid-plane reciprocating probe even up to 20 cm distant from the separatrix, $\Delta_r = 20$ cm. The ion saturation current measured at the probe, j_{sat} is at least as large as values observed at the outboard targets during ELM peaks for $\Delta_r <\sim$ 10–15 cm and is still >10% of the target value at $\Delta_r <\sim$ 20 cm. These interactions may be consistent with the collapse of the density pedestal and formation of an long outboard tail, observed with the high resolution Thomson scattering system in the ELM rise (Section 4.2). They are also observed with the mid-plane linear D_α camera as an asymmetric broadening in the Abel inverted D_α profile, with strong D_α emission (relative to the peak value) being observed at least 5–10 cm into the far outboard SOL.

The magnitude of j_{sat} bursts to the reciprocating probe are rather variable, even for similar size ELMs at the targets, and often no significant increase is observed at all. The bursts have a period much shorter than the period for D_α emission (or ion saturation current) at the target. Typically the reciprocating probe measures periods of less than 50 μs compared to ~300 μs at the target. As a result, 'compound' ELMs at the target are resolved into discrete bursts by the reciprocating probe (e.g. lower panel of Fig. 6), sometimes 3 or 4 during a single ELM event. The j_{sat} bursts are shifted in time with respect to the peak of D_α emission at the targets. When

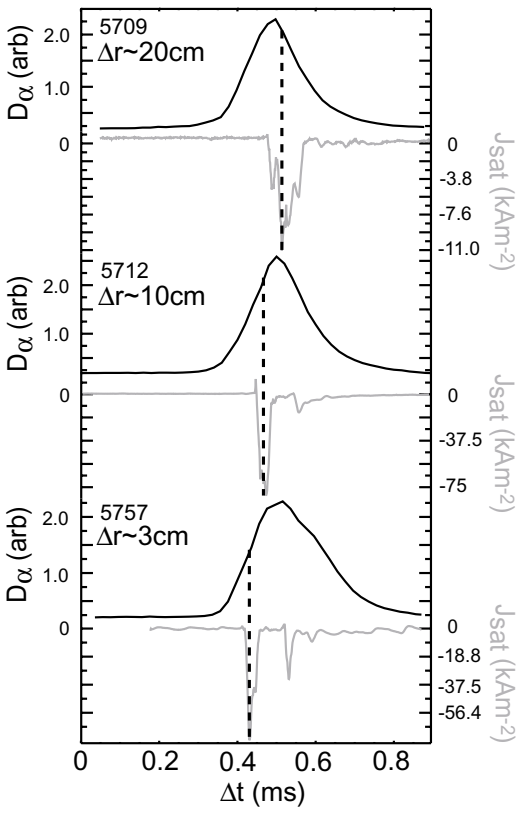

Fig. 6. Target D_α for a single ELM and ion saturation current, j_{sat} from the outboard mid-plane reciprocating probe for three similar shots, with the probe at 3, 10 and 20 cm from the plasma boundary. The time axis has been shifted so that the ELM peak times coincide. The dotted lines represent the time of peak j_{sat} in each shot.

far from the separatrix, $\Delta_r \sim 20$ cm (Fig. 6, top panel), the burst follows the D_α peak by ~20 μs. With the probe at $\Delta_r \sim 10$ cm (Fig. 6, middle panel), the burst precedes the peak by ~40 μs and for the probe close to the separatrix, $\Delta_r \sim 3$ cm (Fig. 6, lower panel), this rises to ~85 μs. These delays appear to be consistent with a radial motion during the bursts at a velocity of around 1.5 km s^{-1}.

As yet the exact nature of the ELM radial effluxes are un-resolved and additional studies are planned. However, the various data appears to be consistent with the radial motion of a high poloidal mode number distortion to the plasma boundary, growing radially at 1–2 km s^{-1}. Apart from toroidally localised diagnostics such as the reciprocating probe, the vessel wall in MAST is remote from the plasma boundary (typically >0.5 m) and there is no obvious interaction during ELMs. However, if radial effluxes of this type exist in tokamaks with a close fitting wall, they could result in substantial interaction with, and erosion of, the plasma facing components far from the divertor region.

5. SOL characterisation and scaling

5.1. Development of scaling for the ST SOL

Target heat loads are determined in large part by the upstream SOL heat flux width, Δ_h. Considerable effort has been made in the past to develop analytical and empirical scalings for Δ_h in existing tokamaks to allow reliable estimates to be made for its magnitude in a next-step device. The derivation of scalings for a large ST such as MAST is particularly important both for development of the ST concept and for improving the robustness of scalings derived for conventional tokamaks since extreme parameter regimes are explored, e.g. in the ratio of ion gyro-radius to Δ_h (which is close to unity in MAST but $\ll 1$ in conventional devices). A first such scaling has been developed for the outboard SOL in MAST CDN plasmas [8].

The scaling was developed for sheath-limited regimes in the SOL by flux-mapping data from the target Langmuir probe arrays to the mid-plane and fitting to key upstream 'engineering' parameters such as P_{SOL}, B_ϕ, $\bar{n}_e$ and the edge safety factor, q_{95}. Only very high quality data (e.g. that taken in the absence of strong MHD in the core plasma and for which the probe characteristics were well fitted by offset exponentials) were included in the dataset used to develop the scaling. In order to minimise the effects of co-linearity, dedicated campaigns were undertaken to explore the widest possible range of each parameter whilst keeping the remainder as fixed as possible. Initial results indicate a good fit to data with a scaling of the form $\Delta_h \propto P_{SOL}^{-0.18} n_e^{0.44} q_{95}^{0.34} B_\phi^{0.96}$. The weak inverse dependence on P_{SOL}, approximately linear dependence on B_ϕ and roughly square root dependence on $\bar{n}_e$ are all fairly robust to different fitting techniques and changes in the dataset. Scalings for the more relevant (to next-step tokamaks) conduction limited SOL are being developed and integration with data from conventional tokamaks is on-going.

5.2. Modelling of the ST SOL

The MAST SOL is being explored using a modified version of the 'OSM2' onion-skin model, part of the 'DIVIMP' package [9]. A detailed comparison of OSM2 modelling in MAST and the conventional tokamak, JET will be published elsewhere [10]. However, one key result is the significance of the mirror force term to the ST SOL. The mirror force is proportional to $\nabla_\parallel B/B$, which is particularly large in the ST due to the low aspect ratio geometry. In the fluid model, OSM2 this term appears as an effective particle and momentum source term and drives strong upstream flows at a significant fraction of the Mach number, M. Preliminary measurements with a Mach probe mounted on the outboard mid-plane reciprocating probe seem to confirm the existence of

upstream flows with $M \sim 0.2$, comparable to OSM2 predictions, although the source for these flows (which could also derive from, for example, $\mathbf{E} \times \mathbf{B}$ drifts in the SOL) has not been confirmed and will require more extensive experiments and further modelling. It is worth noting that, although the mirror term is smaller in conventional tokamaks, comparative modelling of the MAST SOL has shown that it is unlikely to be ignorable. The specific impact of this term has been largely overlooked in modelling of conventional tokamaks and the mirror term may indeed even be absent in some fluid models for the SOL.

6. Target heat load amelioration

6.1. Detachment at the divertor targets

Radiative detachment of the target SOL has been achieved in MAST at both the inboard and outboard targets, for Ohmic plasmas and L-mode plasmas with up to $P_{\mathrm{NBI}} \sim 750$ kW and $I_{\mathrm{p}} \sim 600$ kA. In these plasmas, roll-over of the target j_{sat} occurs at similar $\bar{n}_{\mathrm{e}}$ of $\sim 3.5 \times 10^{19}$ m^{-3} for both the inboard and outboard targets [11]. At $\bar{n}_{\mathrm{e}} \sim 6.5 \times 10^{19}$ m^{-3} the degree of detachment, DOD of the inboard targets is estimated as DOD ~ 20 (from a fit to the conduction limited regime at densities just below $\bar{n}_{\mathrm{e}} \sim 3.5 \times 10^{19}$ m^{-3}, assuming a parabolic dependence of j_{sat} on $\bar{n}_{\mathrm{e}}$). For the same density at the outboard targets, the degree of detachment was lower (as observed on other tokamaks), DOD ~ 6. Detachment was achieved at all four targets despite the fully open nature of the MAST divertor and horizontal outboard targets. Target plasma densities at roll-over are substantially lower than has been reported in other tokamaks, around $n_{\mathrm{t}} \sim 2 \times 10^{18}$ m^{-3} (a consequence of the low $j_{\mathrm{sat}} < 15$ kA m^{-2}) but the existence of detachment is strongly supported by observations of the targets in D_α and D_γ light and in particular by a strong rise in the D_γ/D_α ratio. Efforts to develop a qualitative understanding of the origins of the low n_{t} and how, if at all, this affects the physics underlying the detachment process in MAST are ongoing.

6.2. Asymmetric divertor biasing

Toroidally asymmetric biasing of divertor components in a tokamak has been proposed [12,13] as a means of broadening the target heat flux width by imposing local electric fields of toroidally alternating polarity into the SOL and generating convective cells driven by the changing $\mathbf{E} \times \mathbf{B}$ drift. It was shown theoretically that the magnetic shear present in the vicinity of the X-point would confine these potential perturbations to the divertor region below the X-point, leaving the upstream SOL un-changed (and thus having no deleterious impact on, for example, H-mode access). This technique has the potential to increase the target wetted area, by perhaps a factor 3–5. If successful it could have applications to a next-step device where self-biasing of divertor components could be accomplished by varying the angle (to the magnetic field) or the material (and hence the secondary emission coefficient) of the divertor plates.

An experiment to test the theory was originally planned for the COMPASS-D tokamak but has now been implemented on MAST. Six of the lower divertor ribs were isolated from the vessel and connected to a power supply capable of providing up to 5 kA at 120 V. The ribs were biased positively with respect to the vessel in order to draw an electron current and prevent the applied electric potential from being dropped by the formation of a plasma sheath at the probe surface. The bias potential was applied for 60 ms during the flat top phase of a series of 'identical' 550 kA, Ohmic LSND plasmas and increased on a shot by shot basis from 0 to 120 V. For bias potentials above 80 V, the total current to the six biased ribs remained approximately constant at 3 kA, consistent with the electron current to these ribs being limited by the ion saturation current to the six un-biased ribs in the lower divertor (similar to a large electrostatic double probe in which the six biased and six un-biased ribs form the probe electrodes). Under these conditions, theory predicted that the applied electric field to the biased ribs would be conducted along flux tubes connected to the ribs as required for the formation of potential perturbations in the SOL [13].

During the biased period there were significant changes to the outboard, lower divertor region. As expected from theory, there were no significant changes to any of the other three targets. Most immediately noticable was the change in visible light emission (mostly D_α) from the region, imaged using a 1ms framing rate colour camera. The strike-point location (determined from the peak D_α emission) on the biased ribs was shifted radially outwards by several centimetres (with respect to the natural sweeping of the strike-points introduced by variations in the solenoid fringing field during the shot), whilst those on the un-biased ribs were shifted in the opposite direction (Fig. 7). The formation of a toroidally 'wavy' wetted area such as this is an explicit prediction of the theory and results from the $\mathbf{E} \times \mathbf{B}$ drift between the toroidal field and the electric field imposed on the SOL flux tubes by biasing (the field being in opposite directions on the biased and un-biased ribs). The direction of the strike-point movement was in line with the theoretical prediction.

The width of D_α emission, λ_{D_α} from the strike-point regions on the biased ribs was substantially increased by a factor of around 2.3 and the peak intensity, I_{peak} fell by 30%. The reduction in D_α emission and broadening of

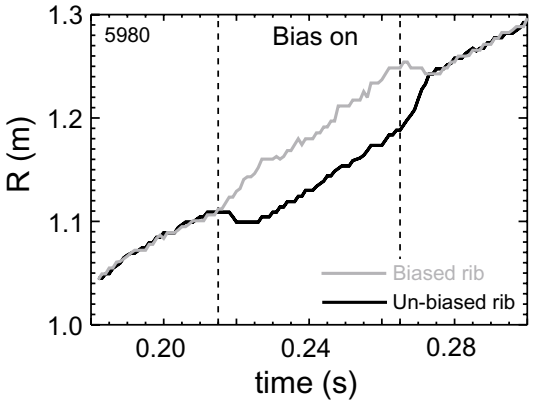

Fig. 7. Radius of the peak in D_α emission for the biased and un-biased divertor ribs around the period in which divertor biasing is applied.

the target footprint are consistent with theory. For this initial experiment, it was not possible to confirm a corresponding impact on the target heat flux width due to the absence of a suitable diagnostic on the biased ribs (such as Langmuir probes or an IR camera view). This will be addressed in future experiments. On the un-biased ribs the impact of biasing was very different, λ_{D_α} narrowed by 40% and I_{peak} rose by a factor 1.4. The target j_{sat} profile also narrowed, by a factor of around 2, although there was no significant change in the peak value. Since the total measured bias current remained constant at ~3 kA, the resultant reduction in total j_{sat} to the un-biased rib must have been compensated for by an increase in that to the biased rib. The total power flowing to the un-biased rib (from analysis of the Langmuir probes) also fell, by more than 25%. The reduction in j_{sat} (away from the strike-point) and power to the target, combined with an increase in D_α emission is reminiscent of phenomena observed during radiative detachment.

These preliminary experiments are very encouraging, in qualitative agreement with theory and demonstrating clear evidence for both SOL broadening and power reduction. There are, however, several aspects of these observations which are not yet understood. Further experiments with improved diagnostics are planned for the future.

7. Summary and conclusions

Recent improvements to the auxiliary heating and gas fuelling systems have broadened the operational space of MAST and, together with a range of new and enhanced diagnostics, has led to a wealth of data on the plasma boundary becoming available.

Operation near to a connected-double null, CDN divertor configuration is found to be very favourable for the ST. H-mode access is significantly eased in CDN and energy losses from the core during ELMs are observed predominantly (>93%) at the outboard targets, which have 40 times the wetted area of the inboard targets. Near CDN both the inter-ELM power flux and ELM energy are well distributed between the upper and lower targets, further reducing target power loading.

The ELMs observed in MAST appear to be Type III, even for the highest auxiliary heating so far supplied to the plasma ($P_{NBI} \sim 2.5$ MW). However, there are indications from stability analysis that these higher power discharges are approaching the ideal ballooning limit where Type I ELMs might be expected. With benign Type III ELMs, MAST achieves high confinement relative to international scalings, $H_H \sim 1$ for ELM frequencies, $f_{ELM} <\sim 100$ Hz simultaneously with high normalised density, $G \sim 0.65$.

During ELMs on MAST, there is a collapse in the steep edge density profile into the far SOL but only moderate changes in temperature profile. ELM losses appear to be dominated by convective transport with a strong correlation to pedestal density but the fractional loss of pedestal energy during ELMs seems un-correlated to pedestal collisionality. The outboard target strike-points move up to 3 cm during low frequency ELMs but there is no significant change in SOL width. The ELMs are also associated with radial perturbations observed up to at least 20 cm from the outboard midplane and which expand radially at around 1.5 km s^{-1}.

Onion skin modelling shows the importance of the mirror force in the MAST SOL, a result of the large $\nabla_\parallel B/B$ in the ST. It is found to drive significant upstream flows, which may have been confirmed by preliminary observations of flows at the outboard midplane at $M \sim 0.2$. Scalings for the SOL heat flux width in MAST are being developed and seem to exhibit the weak inverse dependence on power flow into the SOL observed on conventional tokamaks.

Radiative detachment has been achieved at all four divertor targets in L-mode, with up to $P_{NBI} \sim 750$ kW, despite the open divertor and horizontal outboard targets in MAST. Experiments have also been conducted for the first time to attempt to broaden the SOL in the divertor by toroidally asymmetric biasing of divertor components. The biasing has a strong effect on target D_α and ion saturation current profiles. Initial analysis shows significant broadening of the D_α profile on the biased components and reduction in total heat flux to un-biased components.

Results from MAST are providing a better understanding of the plasma edge and exhaust in the ST and contributing to improved understanding of the physics underlying this region, both for the ST and conventional tokamaks.

Acknowledgements

This work has been jointly funded by EURATOM and UK Department of Trade and Industry. One of the authors, Dr Y. Yang would also like to acknowledge a grant from the Royal Society.

References

[1] G.F. Counsell et al., Plasma Phys. Control. Fusion 44 (2002) 827.
[2] A. Kirk et al., these Proceedings. PII: S0022-3115(02)01541-6.
[3] P.C. Stangeby, The Plasma Boundary of Magnetic Fusion Devices, Institute of Physics, Bristol, 2000, p. 653.
[4] ITER Physics Basis, Nucl. Fusion 39 (1999) 2232.
[5] R. Akers et al., Phys. Plasmas 9 (2002) 3919.
[6] A. Loarte, private communication.
[7] Y. Yang et al., these Proceedings. PII: S0022-3115(02)01574-X.
[8] J.-W. Ahn et al., Contr. Fus., ECA 26B (2002) p1-055.
[9] P.C. Stangeby et al., Nucl. Fusion 28 (1988) 1945.
[10] A. Kirk et al., Plasma Phys. Control. Fusion, to be submitted.
[11] A. Tabasso et al., these Proceedings. PII: S0022-3115(02)01480-0.
[12] R.H. Cohen, D.D. Ryutov, Nucl. Fusion 37 (1997) 621.
[13] D.D. Ryutov, P. Helander, R.H. Cohen, Plasma Phys. Control. Fusion 43 (2001) 1399.